Towards a Fast Non-Empiric Source Model for Installed Rotor Noise

Andrea Franco*
Cluster of Excellence SE²A –Sustainable and Energy-Efficient Aviation, Technische Universität Braunschweig, Germany
Institute of Aerodynamics and Flow Technology, Department of Technical Acoustics, German Aerospace Center (DLR), Lilienthalplatz 7, 38108 Braunschweig, Germany

Roland Ewert†, Michael Mößner‡ and Jan Werner Delfs§
Institute of Aerodynamics and Flow Technology, Department of Technical Acoustics, German Aerospace Center (DLR), Lilienthalplatz 7, 38108 Braunschweig, Germany

The recent demand for sustainable aviation designs challenges aircraft manufacturers to reconsider existing technologies in light of the required cuts in environmental pollution. One of the key factors in addressing these green targets is represented by the integration of unconventional propulsion concepts on the airframe, exploiting electrically driven designs. Among the necessary targets to achieve, a substantial noise emission reduction is needed. Since the new aircraft designs could include existing or novel propulsion system components to address the challenge of reliably predicting noise emissions, in this work a simplified, fast and physical-principles-based rotor noise model is introduced, together with suitable adapted perturbation equations to represent current and possibly newly arising noise sources mechanisms. The rotor noise model is based on rotating point or line sources that represent loading noise in terms of equivalent body forces. The model is applied in a Computational Aeroacoustics (CAA) framework in the time domain. The Linearized Euler Equations (LEE) are split into two separate perturbation equation systems for the acoustic and vorticity mode, respectively. The new noise prediction model, together with the new equations, are implemented in the unstructured quadrature-free experimental Discontinuous Galerkin (DG) CAA solver DISCO++ of DLR. Acoustic Perturbation Equations (APE) describe the propagation of the acoustic mode, and can be discretized numerically very robustly in the DG-framework. The equation split-up intends to overcome numerical stability issues present in the discretization of the LEE with the DG method. The paper reports initial successful results and outlines future possible applications.

I. Introduction

The last decade has seen an increased interest towards sustainable aircraft design concepts, motivated by the need to reduce the environmental impact of aviation. Future aircraft sustainability requirements were translated into an increased number of European and US projects, establishing challenging milestones to be achieved in terms of energy consumption reduction, diminishment in pollutant emissions and perceived noise abatement. To address these goals, aircraft manufacturers are re-evaluating available propulsion technologies and re-designing aircrafts by means of unconventional propulsion integration configurations. Among the most promising new configurations to achieve this goal are distributed electric propulsion systems and buried or semi-buried engine integrations on the airframe. Distributed propulsion concepts would include single or dual fan engines configurations with Boundary Layer Ingestion integrated on blended wing body aircrafts, engines configurations with a common core and multi-fans or propulsors, and more conventional aircraft design with wing-distributed engines arrangements. Buried or semi-buried engines concepts have been proposed for hybrid wing body or blended wing body aircrafts designs.

*Research Scientist, Member AIAA, corresponding author: andrea.franco@dlr.de
†Senior Scientist, Senior Member AIAA
‡Senior Scientist
§Professor, Head of Dept. of Technical Acoustics, Senior Member AIAA

Review contributions on distributed propulsion by Gohardani [1] and hybrid electric propulsion concepts by Wall and Meyer [2] offer a good overview on the state of the art on sustainable aviation technologies. Regardless of the configuration chosen, a requirement to fulfill for future aircraft concepts is a perceived reduction of between 50% and 65% in noise emissions by 2050, based on current technology development. Being new propulsion configurations one of the key aspects in achieving a more sustainable aircraft design, the demanding cut in noise pollution is driving aeroacoustics rotor noise research to provide manufacturers with new design methods, able to predict noise emissions with enough accuracy to be reliably used for new proposed aircrafts noise estimation. The existing propulsion system's components of these new configurations have been studied extensively in the past decades, and their tonal noise sources mechanisms are well understood. The origin of aerodynamic sound generated from a rotor in a subsonic flow has been identified to be originated from both the aerodynamic load on the blades and from the unsteady volume displacement by the blade movement in the flow.

The earliest work of Gutin [3] provides the reference to estimate noise propagation for isolated rotors, treated as rigid devices rotating in a steady uniform flow. However, modern existing rotors during real flight conditions (e.g. forward and transitional flight) show a considerable deviation from the results obtained under such assumptions, due to the highly non-uniform flow and the consequent fluctuating loads during advancement and retreat of the blades. The results provided by Gutin's model show in general an accurate prediction of the fundamental tone, but the predicted higher harmonics differ substantially, due to the missing information about fluctuating loads under non-uniform flows.

Lowson derived a more general analytical expression than Gutin's to evaluate the sound field of a point force singularity in motion, including retarded blade locations and numerical derivatives in the time domain [4], showing that the motion of a fluctuating force will contribute with essentially two components to the sound field generated. One component, dependent on the time rate of change of the force, has a dipole radiation pattern, while the other component is dependent on the acceleration of the system in which the force is acting.

One of the widely used models in present times is the one introduced by Hanson [5], who improved Gutin's model by including also the effects of blade thickness, forward flight, and blade sweep, maintaining the original formulation in the frequency domain. This model represents the state of the art of analytical prediction models for rotor noise.

All the aforementioned models can predict with enough accuracy far-field rotor noise emissions, but near-field noise prediction has revealed to be a complicated task, due to numerous physical phenomena influencing the noise generated. Nevertheless, noise estimation in the vicinity of the blades can be attempted with appropriate physical based simplifications. In Ref. [6] a near-field noise prediction model was presented, with an expression to evaluate the far-field thickness and steady loading noise. This model extends the radiation integrals by an asymptotic analysis for large number of blades. The formulae for the harmonic components of the near-field acoustic pressure show how subsonic blades noise generation results mainly dependent by blade tip aerodynamics, while for supersonic motion, the Ffowcs Williams & Hawkings sonic condition needs to be satisfied by the noise sources to obtain a good estimate.

In parallel to theoretical based models, empirical models to predict rotor noise have also been developed since the beginning of propeller driven aircraft usage. The aim of these methods is to simplify the prediction of far-field and near-field noise while retaining an adequate level of accuracy for aircraft certifications procedures. Various models have been developed until recently and are kept as part of aircraft certification procedures of related agencies such as European Union Aviation Safety Agency and Federal Aviation Administration. All these models are based on approximate equations involving, among the most important parameters, rotor power, RPM, number of blades, flight speed, and rotor diameter. Among the earliest empirical methods based on approximated equations is the one introduced by Smith [7], who proposed an empirical model developed using a regression test analysis from A-weighted sound level data obtained during certification tests of single and twin engines airplanes. In his contribution, Smith included, in addition to the aforementioned model parameters, also blade tip twist and blade thickness, accounting respectively for more correct spanwise loading distributions and thickness noise estimation, the latter being particularly important for high tip speed propellers. Subsequently, purely empirical models are derived or inspired on Smith's approach, which served as the initial reference for empirical models to be used in certification procedures.

Other possible rotor noise estimation approaches combine theoretical simplified results with empirical observations, producing semi-empirical models that serve certifications purposes as well. One such example is the model proposed by Lewy [8] to predict tone noise for Contra Rotating Open Rotors. The model is intended for takeoff and approach conditions characterized by a low advancing Mach number, ensuring subsonic flow conditions at the blades tip. To represent the directivity of a tone, a Bessel function is used, and the overall sound pressure levels are approximated by means of a parabolic pattern. Generally, each of the above mentioned models is able to generate a fairly accurate prediction of the fundamental tone, and provide an estimate of the near-field noise emissions in design-point conditions, but they lack the capability of capturing the correct sound field generated by non-uniform inflow conditions.

Furthermore, even in design-point conditions, an accurate prediction of the higher harmonics is seen as a complex task to be addressed by either analytical or empirical based calculations, and in particular empirical models would have a limited applicability only to existing rotors. In addition to that, future new propulsion configurations would introduce, besides the rotor self-noise contributions, a new type of noise source, arising from the interaction of propulsors with aircraft components. This type of noise source mechanism can be categorized as installation noise, and it is very particular with respect to the propulsion integration configuration chosen. Earliest research on installation noise included investigations on the interaction of a propeller installed on a wing. In Ref. [9], experiments on such configurations were conducted to investigate and quantify the difference in measured noise with respect to an isolated or uninstalled propeller operating under zero inflow angle conditions. The three main installation effects identified and analyzed were the influence of a non-zero inflow angle with respect to the flight path, the distortion of the propeller inflow conditions due to the upwash generated by the presence of wings and flaps behind the propeller, and the interaction of the swirling turbulent propeller slipstream with the wing considered. The combination of such effects was found to produce an increase of 5 to 10 perceived noise decibels compared to non-installed configurations.

In parallel to wing related installation configurations, research concerning the interaction of propellers with empennages, fuselage and pylons showed how the addition of a pylon upstream of the propeller could increase the rotor Blade Passage Frequencies (BPF) of approximately 10 dB, while interaction with fuselage and empennages could increase the BPFs by 3 dB [10]. The inclusion of blowing techniques at the pylon trailing edge could reduce the pylon wake and flow distortion, obtaining blade passage frequencies comparable to those of isolated propellers [11]. If semi-buried engines configurations are considered, the engines stage was found to be characterized by predominantly azimuthal unsteady blade loading with a less periodic tangential velocity variation in the rotor wake. The resulting installation noise sources would present no distinct tonal components and increased broadband noise levels [12].

The particular flow conditions involving new unconventional propulsion configurations, therefore, require methods for noise estimation able to include not only far-field but also near-field prediction capabilities. Given the limitations of the existing-to-date models, due, either to physical modelling simplifications or limited data availability during their development, in this work a new rotor noise prediction method is introduced, which is both fast and physical principles-based.

The concept proposed combines simplified analytical approaches considering rotor blades modelled with rotating singularities within a CAA framework, resulting in a method that is developed on physical principles and is able to address newly designed and already existing propulsion configurations, without requiring a priori empirical knowledge. In addition to the simplicity of its formulation, the model proposed would represent a fast prediction tool to aid the designer in selecting the best aircraft component configuration satisfying the required noise emissions.

To successfully predict installation noise sources, the model under development would require appropriate underlying equations to describe the flow physics mechanisms giving rise to the previously mentioned excess noise. A suitable system of equations for this purpose would the LEE, containing acoustic and vortical modes, whose interaction is believed to be responsible for the generation of noise sources categorizable as installation noise sources. LEE have been extensively studied for aeroacoustics analysis of turbomachinery noise and exterior noise, and they have been among the most important equations for CAA applications for decades. These equations have been successfully applied in a various range of applications using finite difference discretization. An overview of the state-of-the-art finite difference methods for CAA can be found in [13], where references to relevant successful applications are reported. Nevertheless, LEE are not free from instabilities such as the unbounded Kelvin- Helmholtz type, therefore more robust systems of equation are needed for acoustic computations, representing acoustic and vortical modes appropriately.

The work of Goldstein [14] served as the basis for subsequent formulations of perturbation equations based on velocity split approaches. It extended the Rapid Distortion Theory of Hunt [15] showing that, in an unsteady, compressible isentropic and vortical flow, the velocity can be written as the sum of the gradient of a perturbation potential and an incident distortion velocity, with the perturbation in pressure obtained as the convective derivative of the perturbation potential. The perturbation potential would result from the solution of a linear inhomogeneous wave equation including a dipole source term dependent on the incident distortion velocity.

Later developments by Atassi and coworkers, inspired by Goldstein's findings, showed how a different velocity splitting approach, in which the vector of the velocity fluctuations is decomposed in vortical, entropic and potential components, could be employed to study turbomachinery stage noise. For a uniform background mean flow, such components would result uncoupled from mean flow effects, allowing to study them separately through the corresponding fundamental eigensolutions, pertaining to distinct equations. In a non-uniform flow, the above-mentioned fluctuating components would become coupled, and the corresponding eigensolutions would be not purely representative of each single component.

The initial work of Kerrebrock [16] was continued in Ref. [17], showing how the interaction of flow disturbances with a non-uniform mean flow gives rise to non-distinct eigenmodes. The non-distinct potential, entropic and vortical modes of the flow disturbances would arise due to the centrifugal and Coriolis forces generated by the non-uniform mean flow considered. By studying a mean swirling flow in an annular duct, it was shown how two set of coupled eigenmodes could be identified to be describable as predominantly vorticity-dominated and pressure-dominated, but not solely referring to a single velocity fluctuation split component. The pressure-dominated eigenmodes would contain a fraction of vorticity, while the vorticity-dominated eigenmodes would be associated with a small pressure as well. Subsequently, the velocity splitting approach has been successfully applied to fan engine noise estimation, in particular in the study of noise arising from the interaction of rotor wakes with outlet guide vanes [18][19]. Analytical models based on a split approach for related engineering problems have also been proposed by Peake and coworkers in Ref. [20][21].

Motivated by the successful results obtained by a split-methods to investigate acoustic and vortical modes interactions for turbomachinery rotors and by the recent work of Wohlbrandt [22] and Ewert [23], in this paper, a similar concept is also applied to the LEE, under isentropic flow conditions. This simplification is motivated by the typical subsonic Mach number range of applications for sustainable propulsion related designs.

A coupled system of equations is applied in this work based on APE [24] for the acoustic propagation part and a strictly derived additional transport equation for the non-potential component of the velocity fluctuations. The APE have demonstrated to provide a robust numerical method for acoustic computations, specifically also in combination with DG discretization.

The subject of this work would be the rotor noise model in combination with the newly proposed system of equations. Through this choice, the computational cost of the CAA simulations to predict future applications involving propulsion related installation noise is reduced at an acceptable level of accuracy. In a previous paper [25], a similar approach was considered in the DLR CAA finite difference code PIANO, where the LEE were the only considered governing equations. In this work, initial results of the implementation of both the rotor model and the equations' system in the unstructured quadrature-free DG CAA solver DISCO++ of DLR are reported.

II. Rotor Source Noise Model Implementation

The rotor source noise model is based on rotating singularities and line source distributions, representative of loading noise contributions. The modelling approach considered allows to simulate a rotor without the necessity of defining moving surfaces or the exact blade geometry in the CAA simulations.

A. Calculation of the Time Dependent Sources Location

Each rotor blade is replaced either by a single source singularity, or a distribution of sources along a three-dimensional line, which rotate uniformly around the specified rotor axis as the computational time advances. To prescribe the sources, the high-order points coordinates of the computational grid are transformed in a local cylindrical coordinate system, with its center located at the hub of the corresponding physical rotor being modelled, The location of the singularities or of the line-distributed sources is initially defined as $\boldsymbol{X_{init}} = (r_{init}, \phi_{init}, x_{init})^T$. The circumferential coordinate ϕ_{time}, describing the time dependent source location, is computed from the source's Revolutions Per Second n prescribed in input. Multiple rotor blades N_{blade} are defined assuming equi-spaced blades determined by a circumferential offset $2\pi/N_{blade}$ applied to ϕ_{time}. Figure 1 and 2 present the rotor model geometrical quantities of interest, respectively for a point and line source distribution.

For a rotating singularity, the sources' values would be defined by the integrated load vector $\boldsymbol{f} = (f_r, f_\phi, f_x)^T$, whereas for a line source distribution the values would be defined by integrated blade surface loads at multiple radial locations r_i from existing actuator disk Reynolds Averaged Navier Stokes (RANS) or unsteady RANS rotor simulations, or by simplified Blade Element Momentum (BEM)-based theories. The load values are included appropriately in the sources vector $\boldsymbol{S} = (S_i)^T$, where i depends on the perturbation equation of interest.

B. Regularization of Sources

The definition of a single or line distributed singularity in space-discretized schemes such as the DG-method considered in this work, is frequently causing numerical instabilities. Therefore, an approximation by distributed values is required, which is obtained by regularising on the grid the sources values of coordinates $\boldsymbol{r_{Source}} = (r_{Source}, \phi_{Source}, x_{Source})^T$ using a Gaussian kernel, so that the prescription of sources in the computational mesh described by $\boldsymbol{r_{Grid}} = (r_{Grid}, \phi_{Grid}, x_{Grid})^T$ is easily accomplished.

For a source singularity, a 3D isotropic Gaussian kernel $K(\boldsymbol{r_{Source}}, \boldsymbol{r_{Grid}})$ is considered, which reads as:

$$K(\boldsymbol{r_{Source}}, \boldsymbol{r_{Grid}}) = \left(\frac{ln(2)}{\pi}\right)^{\frac{3}{2}} \frac{1}{\varepsilon^3} \exp\left(\frac{-ln(2)d_{PntSrc}^2}{\varepsilon^2}\right) \tag{1}$$

where $d_{PntSrc} = |\boldsymbol{r_{Source}} - \boldsymbol{r_{Grid}}|$ is the distance between the current position of the singularity in motion and a grid point, and ε is the half-width at half-maximum, representing the distance over which the Gaussian distribution drops from the maximum value to half its maximum.

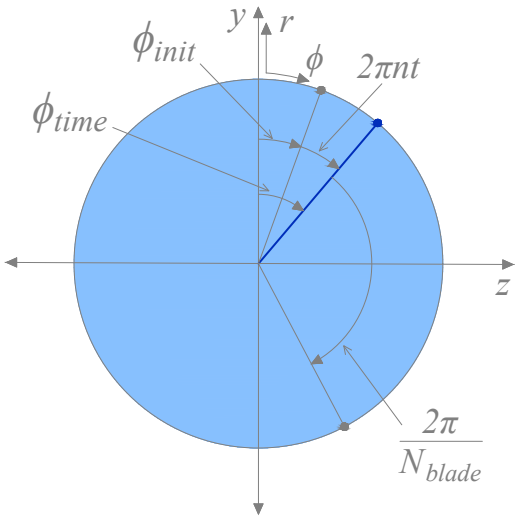

Fig. 1 Rotor cylindrical coordinate system for a source singularity

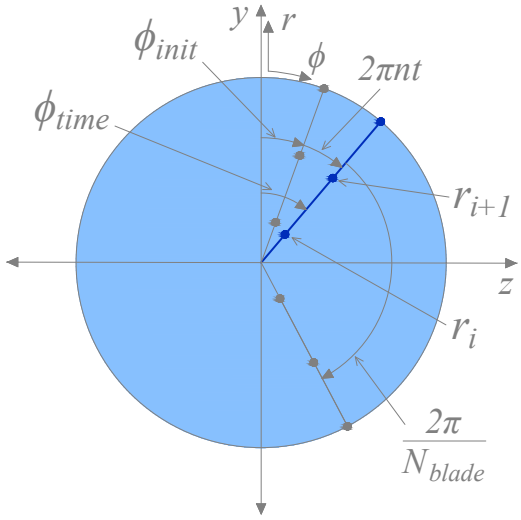

Fig. 2 Rotor cylindrical coordinate system for a line-distributed source

For a line-distributed source, the radial source values along the line are already known from the source prescribed in input, therefore the source value is obtained in this case as the result of a two-step procedure. First, the value at a given radial location r_{Grid} in the computational grid is linearly interpolated from the values in input, within the appropriate range $[r_i, r_{i+1}]$, obtaining $\boldsymbol{f_{Interp}} = (f_{Interp,r}, f_{Interp,\phi}, f_{Interp,x})^T$.

As a second step, the value of the prescribed source at a given radial location in the computational grid is considered a known quantity, equivalent to $f_{Interp,r}$, reducing the necessary dimensions over which regularising is required. Therefore, the regularization kernel $K(\phi_{Source}, x_{Source}, \phi_{Grid}, x_{Grid})$ considered for the case of a line source distribution is applied to $\boldsymbol{f_{Interp}}$ and defined as:

$$K(\phi_{Source}, x_{Source}, \phi_{Grid}, x_{Grid}) = \left(\frac{ln(2)}{\pi}\right) \frac{1}{\varepsilon^2} \exp\left(\frac{-ln(2)d_{LineSrc}^2}{\varepsilon^2}\right) / \mathrm{erf}\left(\frac{\pi\sqrt{(ln(2))}r_{Source}}{\varepsilon}\right) \tag{2}$$

where $d_{LineSrc} = \sqrt{r_{Source}^2(\phi_{Source} - \phi_{Grid})^2 + (x_{Source} - x_{Grid})^2}$ is the distance on a cylindrical surface at a given radius r_{Source}, with ϕ_{Source} the line source azimuthal location, ϕ_{Grid} the grid point azimuthal coordinate, x_{Source} the line source axial location, x_{Grid} the grid point axial coordinate. ε is the half-width at half-maximum of the Gaussian kernel. The Gaussian kernel $K(\phi_{Source}, x_{Source}, \phi_{Grid}, x_{Grid})$ is derived from a 2D Gaussian Kernel independent of the r coordinate, and averaged with an integration over the circumference, so that the resulting projected source, if integrated over the computational domain, would correspond to the source value prescribed in input. The integration results in the error function term erf appearing at the denominator of $K(\phi_{Source}, x_{Source}, \phi_{Grid}, x_{Grid})$, which for a given radius r_{Source} provides a constant scale factor.

The regularized source values, described as the sum of a steady mean and a fluctuating component, need to be further manipulated, in order to obtain the required fluctuating source components to be included in the perturbation equations of interest. The steady mean value $\boldsymbol{S_{mean}}$ to be subtracted from the input source values is obtained by integrating over a circle the Gaussian regularized source. The fluctuating component is therefore obtained as $\boldsymbol{S'} = \boldsymbol{S} - \boldsymbol{S_{mean}}$, and after being scaled for the perturbation equation of interest, it is transformed back into the initial high-order points coordinate system and assigned to the appropriate point of the DG discretization.

III. System Of Perturbation Equations

In combination with the rotor noise model, in this work, a newly defined system of equations is introduced to appropriately represent the interaction of acoustic and vortical eigenmodes, which is at the same time robust enough for applications including complex geometries. The system of equations is derived from the LEE, presented here in their primitive variables formulation:

$$\frac{\partial \rho'}{\partial t} + \nabla \cdot (\rho_0 \boldsymbol{u'} + \rho' \boldsymbol{u_0}) = \dot{\theta}' \tag{3}$$

$$\frac{\partial \boldsymbol{u'}}{\partial t} + (\boldsymbol{u_0} \cdot \nabla)\boldsymbol{u'} + (\boldsymbol{u'} \cdot \nabla)\boldsymbol{u_0} + \frac{\nabla p'}{\rho_0} - \rho' \frac{\nabla p_0}{\rho_0^2} = \frac{\boldsymbol{f'}}{\rho_0} \tag{4}$$

$$\frac{\partial p'}{\partial t} + \boldsymbol{u_0} \cdot \nabla p' + \boldsymbol{u'} \cdot \nabla p_0 + \gamma p_0 \nabla \cdot \boldsymbol{u'} + \gamma p' \nabla \cdot \boldsymbol{u_0} = \frac{c_0^2}{\gamma} \dot{\theta}' \tag{5}$$

where ρ, $\boldsymbol{u}$, p, t, and γ are respectively the density, velocity, pressure, time, and specific heat ratio of air, with subscript 0 indicating mean flow quantities and primed symbols indicating perturbation quantities. On the assumption of isentropic flow conditions, the linearized expression $p' = \rho' c_0^2$ is introduced, with c_0 as the speed of sound computed from the mean flow, and Eq. (3) is rewritten as:

$$\frac{\partial p'}{\partial t} + c_0^2 \nabla \cdot \left(\boldsymbol{u_0} \frac{p'}{c_0^2} + \rho_0 \boldsymbol{u'} \right) = c_0^2 \dot{\theta}' \tag{6}$$

Being entropy a known quantity, the first-order formulation $p' = \rho' c_0^2$ describes completely the relation between pressure and density perturbations, so that Eq. (5) can be replaced by Eq. (6), and Eq. (3) by Eq. (9), obtaining the isentropic formulation of the LEE (LEE-s).

$$\frac{\partial p'}{\partial t} + c_0^2 \nabla \cdot \left(\boldsymbol{u_0} \frac{p'}{c_0^2} + \rho_0 \boldsymbol{u'} \right) = c_0^2 \dot{\theta}' \tag{7}$$

$$\frac{\partial \boldsymbol{u'}}{\partial t} + (\boldsymbol{u_0} \cdot \nabla)\boldsymbol{u'} + (\boldsymbol{u'} \cdot \nabla)\boldsymbol{u_0} + \nabla \left(\frac{p'}{\rho_0} \right) = \frac{\boldsymbol{f'}}{\rho_0} \tag{8}$$

$$\rho' = \frac{p'}{c_0^2} \tag{9}$$

A decomposition is then applied to the perturbation velocities $\boldsymbol{u'}$ of Eq. (8), which reads as:

$$\boldsymbol{u'} = \boldsymbol{u^a} + \boldsymbol{u^r} \tag{10}$$

The decomposition at this stage in the derivation is not uniquely defined. To characterize $\boldsymbol{u^a}$ to correspond to the acoustic velocity perturbation, an additional condition is imposed prescribing the unsteady pressure only in terms of the unsteady potential φ, as in Eq. (11).

$$p' = -\rho_0 \frac{D_0 \varphi}{Dt}, \qquad \frac{D_0}{Dt} := \left\{ \frac{\partial}{\partial t} + \boldsymbol{u_0} \cdot \nabla \right\} \tag{11}$$

The obtained velocity $\boldsymbol{u^a} = \nabla \varphi$ describes the potential (acoustic) component, while $\boldsymbol{u^r}$ is the non-acoustic component, which incorporates the solenoidal field descending from the LEE as well. Introducing the decomposition of Eq. (10) in Eq. (8), and shifting on the right-hand-side the terms related to the pressure perturbation and to the $\boldsymbol{u^a}$ component, the decomposed momentum equation reads as:

$$\frac{\partial \boldsymbol{u^r}}{\partial t} + (\boldsymbol{u_0} \cdot \nabla)\boldsymbol{u^r} + (\boldsymbol{u^r} \cdot \nabla)\boldsymbol{u_0} = -\left(\frac{\partial \boldsymbol{u^a}}{\partial t} + (\boldsymbol{u_0} \cdot \nabla)\boldsymbol{u^a} + (\boldsymbol{u^a} \cdot \nabla)\boldsymbol{u_0} + \nabla \left(\frac{p'}{\rho_0} \right) \right) + \frac{\boldsymbol{f'}}{\rho_0} \tag{12}$$

The right-hand-side of Eq. (12) is re-written further, using the mathematical identity for the $\boldsymbol{u^a}$ component:

$$(\boldsymbol{u_0} \cdot \nabla)\boldsymbol{u^a} + (\boldsymbol{u^a} \cdot \nabla)\boldsymbol{u_0} = \nabla(\boldsymbol{u^a} \cdot \boldsymbol{u_0}) + \boldsymbol{\omega^a} \times \boldsymbol{u_0} + \boldsymbol{\omega_0} \times \boldsymbol{u^a} \tag{13}$$

where the term $\boldsymbol{\omega^a} \times \boldsymbol{u_0} = (\nabla \times \boldsymbol{u^a}) \times \boldsymbol{u_0} = \boldsymbol{0} \times \boldsymbol{u_0} = \boldsymbol{0}$ can be simplified due to the irrotationality of the velocity component $\boldsymbol{u^a} = \nabla\varphi$. The resulting equation reads as:

$$\frac{\partial \boldsymbol{u^r}}{\partial t} + (\boldsymbol{u_0} \cdot \nabla)\boldsymbol{u^r} + (\boldsymbol{u^r} \cdot \nabla)\boldsymbol{u_0} = -\left(\frac{\partial \boldsymbol{u^a}}{\partial t} + \nabla(\boldsymbol{u^a} \cdot \boldsymbol{u_0}) + \nabla\left(\frac{p'}{\rho_0}\right)\right) + \frac{\boldsymbol{f'}}{\rho_0} - \boldsymbol{\omega_0} \times \boldsymbol{u^a} \tag{14}$$

It is possible to verify that the right-hand-side term of Eq. (14) highlighted in brackets can be obtained also from Eq. (11), by dividing the terms of the equation by ρ_0, and taking the gradient of each term, substituting in the end $\nabla\varphi = \boldsymbol{u^a}$. The resulting equation reads as:

$$\frac{\partial \boldsymbol{u^a}}{\partial t} + \nabla(\boldsymbol{u^a} \cdot \boldsymbol{u_0}) + \nabla\left(\frac{p'}{\rho_0}\right) = \boldsymbol{0} \tag{15}$$

and it represents the left-hand-side of the momentum equation of the APE [24].

Equation (15) can then be substituted in Eq. (14), obtaining:

$$\frac{\partial \boldsymbol{u^r}}{\partial t} + (\boldsymbol{u_0} \cdot \nabla)\boldsymbol{u^r} + (\boldsymbol{u^r} \cdot \nabla)\boldsymbol{u_0} = +\frac{\boldsymbol{f'}}{\rho_0} - \boldsymbol{\omega_0} \times \boldsymbol{u^a} \tag{16}$$

The momentum equation for $\boldsymbol{u^r}$, multiplied by ρ_0, is further re-written in a conservative form, adding to it the mean flow field continuity equation, multiplied by $\boldsymbol{u^r}$:

$$\rho_0\frac{\partial \boldsymbol{u^r}}{\partial t} + \rho_0(\boldsymbol{u_0} \cdot \nabla)\boldsymbol{u^r} + \rho_0(\boldsymbol{u^r} \cdot \nabla)\boldsymbol{u_0} + \boldsymbol{u^r}\left(\frac{\partial \rho_0}{\partial t} + \nabla \cdot (\rho_0\boldsymbol{u_0})\right) = \boldsymbol{f'} - \rho_0\boldsymbol{\omega_0} \times \boldsymbol{u^a} \tag{17}$$

The two terms $\boldsymbol{u^r}\nabla \cdot (\rho_0\boldsymbol{u_0})$ and $\rho_0(\boldsymbol{u_0} \cdot \nabla)\boldsymbol{u^r}$ can be re-written as $\nabla \cdot (\rho_0\boldsymbol{u_0}\boldsymbol{u^r})$, obtaining in the end the final conservative form of the linearized momentum equation for $\boldsymbol{u^r}$, which reads as:

$$\frac{\partial(\rho_0\boldsymbol{u^r})}{\partial t} + \nabla \cdot (\rho_0\boldsymbol{u_0}\boldsymbol{u^r}) + \rho_0(\boldsymbol{u^r} \cdot \nabla)\boldsymbol{u_0} = \boldsymbol{f'} - \rho_0\boldsymbol{\omega_0} \times \boldsymbol{u^a} \tag{18}$$

Introducing also Eq. (10) into Eq. (7), the final form of the system of equations is:

$$\frac{\partial p'}{\partial t} + c_0^2\nabla \cdot \left(\boldsymbol{u_0}\frac{p'}{c_0^2} + \rho_0\boldsymbol{u^a}\right) = -c_0^2\nabla \cdot (\rho_0\boldsymbol{u^r}) + c_0^2\dot{\theta}' \tag{19}$$

$$\frac{\partial \boldsymbol{u^a}}{\partial t} + \nabla(\boldsymbol{u^a} \cdot \boldsymbol{u_0}) + \nabla\left(\frac{p'}{\rho_0}\right) = \boldsymbol{0} \tag{20}$$

$$\frac{\partial(\rho_0\boldsymbol{u^r})}{\partial t} + \nabla \cdot (\rho_0\boldsymbol{u_0}\boldsymbol{u^r}) + \rho_0(\boldsymbol{u^r} \cdot \nabla)\boldsymbol{u_0} = -\rho_0\boldsymbol{\omega_0} \times \boldsymbol{u^a} + \boldsymbol{f'} \tag{21}$$

The LHS of Eq. (19) and Eq. (20), without the source term $-c_0^2\nabla \cdot (\rho_0\boldsymbol{u^r})$, is equivalent to the APE [24]. Equations (19) and (20) predict the propagation of acoustic modes over a non-uniform medium. In addition to the APE, Eq. (21), hereafter referred to as Vortical Convection Equation (VCE), represents the convection of non-acoustic velocity perturbations on a background mean flow. The system of equations is named APE+VCE, and is equivalent to the LEE-s, as it can be verified by adding Eq. (20) with Eq. (21). If a non-uniform medium is considered, the velocities decomposition would not provide exactly distinct potential and solenoidal components of the velocity, as described in [17]. As a consequence, the resulting decomposition is general and suitable to be used for installation noise prediction purposes, with non-distinct vortical and acoustic eigensolutions. The source terms of the LEE can be assigned to Eq. (19) for externally prescribed mass sources, and to Eq. (21) for externally prescribed fluctuating forces.

At this development stage, the term $+\rho_0(\boldsymbol{u^r} \cdot \nabla)\boldsymbol{u_0}$ is neglected since it is the source for hydrodynamic instabilities. The term $-\rho_0\boldsymbol{\omega_0} \times \boldsymbol{u^a}$ is also not considered in the discretized equations, since it represents a feedback from acoustics to the entropy mode, which is assumed to not be relevant for installation noise configurations. The resulting APE+VCE system of equations with the terms $+\rho_0(\boldsymbol{u^r} \cdot \nabla)\boldsymbol{u_0}$ and $-\rho_0\boldsymbol{\omega_0} \times \boldsymbol{u^a}$ neglected is the system of perturbation equations used in this work, introduced to overcome fundamental robustness difficulties of the LEE for DG discretizations. For applications purposes, the velocity decomposition Eq. (10) allows to separate the possible sources of instabilities in a dedicated equation. The neglected mean flow terms $+\rho_0(\boldsymbol{u^r} \cdot \nabla)\boldsymbol{u_0}$ and $-\rho_0\boldsymbol{\omega_0} \times \boldsymbol{u^a}$ avoid potential physical instabilities that could arise from configurations to be investigated. The resulting VCE equation is a convection equation for the variable $\rho_0\boldsymbol{u^r}$, which could still present numerical instabilities for certain prescribed mean flow definitions.

To realize a robust system of equations, the VCE can be easily stabilized by application of suitable numerical limiting techniques. Currently a limiter adapted from maximum-principle-satisfying formulations is implemented, which limits $\rho_0 \boldsymbol{u}^r$ within a range defined by the maximum and minimum initial solution values.

IV. Validation

The proposed modelling approach combining the APE+VCE system of equations with the rotating point and line sources model has been validated for an isolated propeller, with prescribed regularized singularities as well as line sources distributions of forces representative of a realistic thrust distribution. From the results obtained, a suitable setup for a realistic installed configurations was identified, and a comparison with an isolated propeller configuration is described, demonstrating the prediction capabilities of the model.

All the simulations were performed with the experimental DG CAA solver DISCO++ of DLR, where the newly proposed APE+VCE system of equations is solved on a tetrahedral grid. In each tetrahedron, the solution is represented with a third order polynomial. Time integration is performed with a fourth order Runge-Kutta method.

A. Force Singularity

Initially, the results of a single rotating force singularity are analyzed to identify an appropriate set of parameters for the regularized source prescribed in input. The computational domain used for these tests is sketched in Fig. 3. Table 1 summarizes the main simulation input parameters

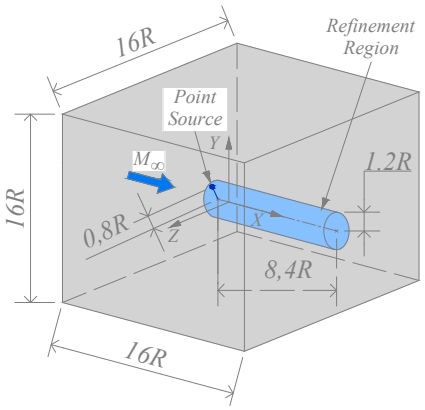

Fig. 3 Computational domain for the source singularity test cases

Table 1 Simulations Input Parameters

Input Parameter	Value
Free-stream Mach nr. M_∞	0.17
n	218.77 s^{-1}
Propeller Blade Length R	0.2032 m
Thrust	75.18 N
Farf. Tetra Cell Size Δx_{Far}	0.3224
Refin. Tetra Cell Size Δx_{Ref}	0.03224
Number of Time Steps	200,000
Time Step Size	0.0001

The source singularity regularized with Eq. 1 is resolved in the computational grid inside a cylindrical refinement region, with a radial extension chosen to appropriately resolve the area of vortex propagation, as well as to avoid spurious numerical noise that might arise from a sharp transition in grid cells' size. The rotating source is defined in a y-z plane centered at $(x, y, z) = (-0.4, -0.15, 0.0)$.

The tetrahedral cells size of the computational domain in the farfield is defined to resolve the first ten harmonics. The chosen grid size in the refinement region is reduced to 1/10 of the farfield tetrahedral edge length. To describe more accurately blade loading effects for a propeller, the singularity is placed in the refinement region at 0.8R in the radial direction.

On the domain outer surfaces, a non-reflecting boundary condition is applied, formulated on an upwind flux vector splitting approach, with prescribed null incoming eigenmodes. The computational time corresponds approximately to five complete revolutions of the rotating singularity.

All the subsequent results are presented in terms of Sound Pressure Level (SPL), considering a ratio of $\varepsilon/\Delta x_{Ref} = 2$, for a better regularized source resolution on the computational grid. The energy content of the solution is described considering the 1st, 3rd, and 5th frequency mode of the fluctuating pressure signals, captured on the x-y coordinate plane with virtual microphones, placed at a distance of 4R from the origin of the propeller's cylindrical coordinate system.

The results obtained from the CAA simulations are compared with known closed form solutions of the wave equation describing the perturbation pressure field of a rotating singularity in a uniform flow.

Equation (22) describes the solution for a force singularity.

$$p'_{f_p}(\boldsymbol{x},t) = \frac{1}{4\pi}\left\{\frac{\frac{\partial \boldsymbol{f_p}}{\partial \tau}\cdot \boldsymbol{e_R} + (\boldsymbol{f_p}\cdot \boldsymbol{e_R})\frac{\partial \boldsymbol{M_q}}{\partial \tau}\cdot \boldsymbol{e_R}(1-M_{qR})^{-1}}{a_\infty R_i(1-M_{qR})^2}\right\} + + \frac{1}{4\pi}\left\{\frac{-\boldsymbol{f_p}\cdot \boldsymbol{M_q} + (1-\boldsymbol{M_q}^2)\boldsymbol{f_p}\cdot \boldsymbol{e_R}(1-M_{qR})^{-1}}{R_i^2(1-M_{qR})^2}\right\}$$

$\boldsymbol{M_q}$ represents the Mach number of the source in motion, $\boldsymbol{x}$ the observer position, $\boldsymbol{y(\tau)}$ the singularity position dependent on the retarded time τ, $R_i = |\boldsymbol{R_i}| = |\boldsymbol{x} - \boldsymbol{y(\tau)}|$ the distance between source and observer, $\boldsymbol{e_R} = \boldsymbol{R_i}/R_i$ the unit distance vector between source and observer, $\boldsymbol{M_{qR}} = \boldsymbol{M_q}\cdot \boldsymbol{e_R}$ the momentary Mach number component in the direction of the observer, and a_∞ the speed of sound. If a uniform flow is considered, the distance R_i will change as $R_i = |\boldsymbol{R_i}| = |\boldsymbol{x} - \boldsymbol{y(\tau)} - \boldsymbol{U_\infty}(\tau - t)|$, and the Mach number will change as well as $\boldsymbol{M_q} = \boldsymbol{M_q} + \boldsymbol{U_\infty}$, with $\boldsymbol{U_\infty}$ representing the free stream velocity vector. The results of the simulated thrust force with the APE+VCE system of equations are examined qualitatively in Fig. 4, where the fundamental expected features from the simplified test case investigated can be recognized.

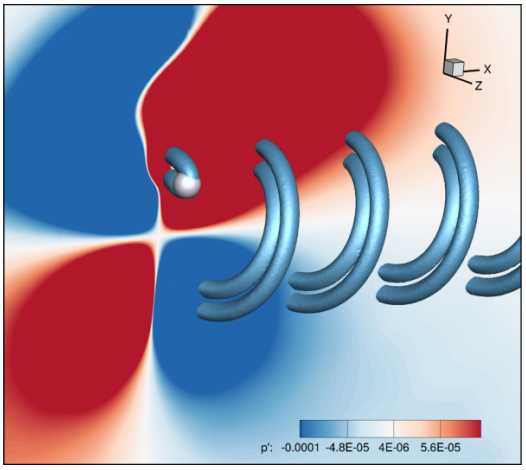

Fig. 4 Contour plot of p' for simulated thrust singularity, with Q-Criterion superimposed

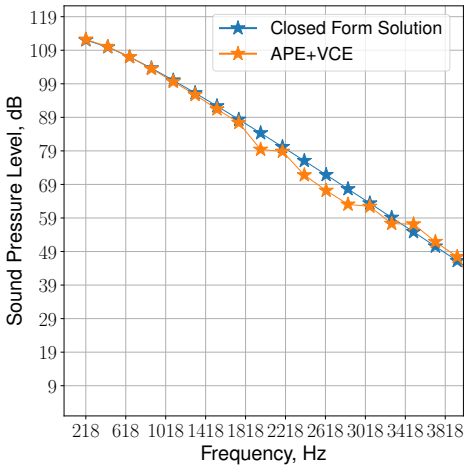

Fig. 5 Narrow band spectrum of p', simulated thrust, $M_\infty = 0.17$.

The proposed system of equations describes well the radiated sound pattern, presented in terms of pressure fluctuations contour. Quadrupole-type pressure fluctuation patterns can be observed. Due to the rotation of the force singularity, a ring vortex pattern is identifiable from the Q-Criterion iso-surfaces, superimposed on the perturbation pressure contour. Propeller noise prediction-methods are required to capture the logarithmic decreasing trend of the harmonics as well. Figure 5 shows the narrow band spectrum of the fluctuating pressure signal at a location of 45°, obtained simulating a thrust force with $M_\infty = 0.17$. A single harmonic is represented in the plot by a corresponding marker. For the first 10 harmonics, the SPL values in dB decrease rapidly as expected, with higher harmonics being investigated. Large SPL values are identifiable for frequencies higher than 2200 Hz, which might be due to a limited mesh resolution or spurious numerical noise.

In addition to the previous results, a sensitivity study was performed for different ratios $\varepsilon/\Delta x_{Ref}$, simulating a single thrust force source in the APE+VCE equations with $M_\infty = 0.17$, as shown in Fig. 6. The purpose of this study is to identify a suitable reference for sources regularization, that would maintain on one side the properties of a mathematical singularity, but at the same time could also be incorporated in the computational mesh.

The results for the 1st mode present louder levels at around 45° in the first quadrant, with symmetrical values in other quadrants. Higher modes are characterized by a shift of the maximum levels location towards 90° and 270°. From the analysis of the results of the 1st mode, the energy content is seen not to depend on the choice of $\varepsilon/\Delta x_{Ref}$.

The examination of the directivity of the 3rd mode shows that the SPL becomes sensitive towards $\varepsilon/\Delta x_{Ref}$ ratios, indicating how larger values of $\varepsilon/\Delta x_{Ref}$ would influence the higher harmonics. When analyzing the results of the 5th mode, different $\varepsilon/\Delta x_{Ref}$ accentuate the differences seen from the investigation of the results of the 3rd Mode: values up to $\varepsilon/\Delta x_{Ref} = 4$ show similar levels, whereas, higher $\varepsilon/\Delta x_{Ref}$ produce a reduction in SPL.

The sensitivity study performed highlights how a singularity, regularized over several computational grid points, would cause a modification of the radiated sound wave and a non-negligible reduction in its energy content. The location of the microphones was defined at a distance 4R to avoid near-field effects on the solution. From the SPL of the 5th mode, axial noise emission is detectable, indicating the presence of numerical noise otherwise not present from analytically predicted results.

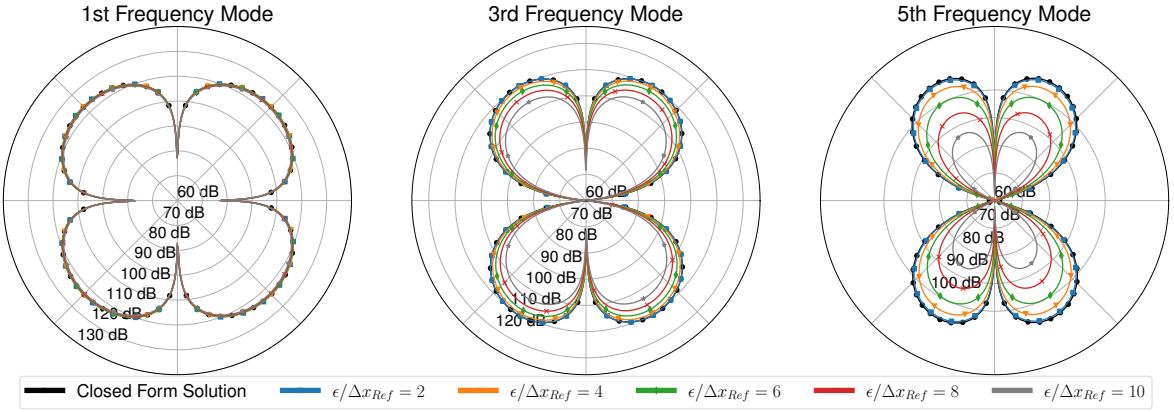

Fig. 6 SPL (dB) for different $\varepsilon/\Delta x_{Ref}$. Simulated thrust with $M_\infty = 0$.

The equivalence of the APE+VCE with the LEE-s and LEE, as stated in Section III, is verified with a simplified test case simulating a thrust force singularity with $M_\infty = 0.17$. In Fig 7, the results in terms of SPL polar directivities show a comparison of these equations with the APE solution and the equivalent closed form solution provided by Eq. (22).

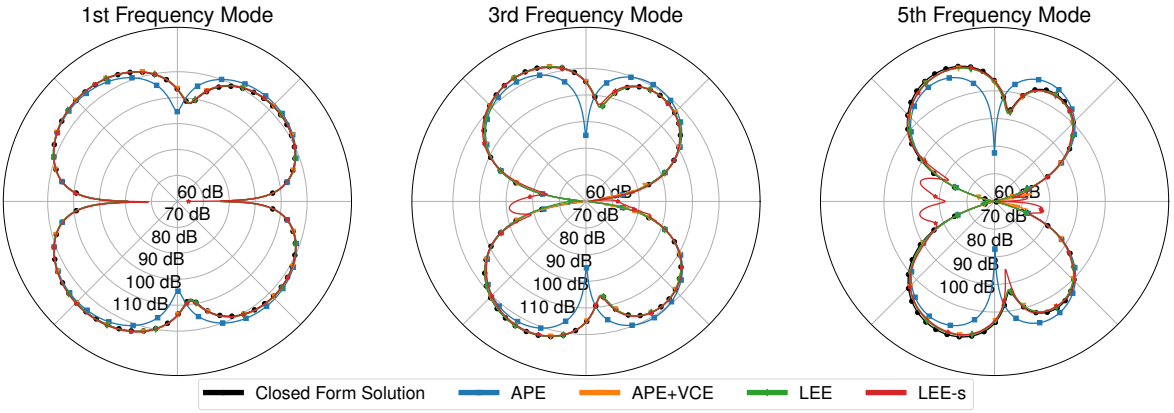

Fig. 7 SPL (dB) equations comparison. Results of a simulated thrust with $M_\infty = 0.17$.

The results of all the equations, except for the case of APE, show a very good agreement of the SPLs for the 1st mode. The Doppler shift of the directivity pattern, that would be expected from this simulation, is not seen in the APE results. The explanation for the obtained APE results is due to the filtering of entropical and vortical modes applied in their formal derivation: to restore the correct prediction of the pressure signal, the APE would require a filtered source equivalent to the gradient of the potential component of the force perturbation. In the APE+VCE system of equations, the filtered source definition is highlighted by the source term present in the equation for the perturbation pressure. The analysis for the 3rd and 5th frequency mode maintains overall a very good agreement, APE results aside. Excess noise is detectable in the region near the axis of rotation of the singularity, which could be explained as previously done for Fig. 6.

From the analysis of the force singularity test cases, the assumptions made on the newly defined APE+VCE system of equations are verified, and a value of $\varepsilon/\Delta x_{Ref} = 2$ has been identified as providing a good compromise between regularized source and singularity representation.

B. Line-Distributed Force

Although singularities-based models have been successfully applied for rotor noise emission prediction, blade surface loads representation by means of a single integrated value would not provide a realistic representation of a rotor blade and its local flow effects on the surrounding medium, including the generated acoustic response. For this reason, a more advanced representation of rotor blades by means of line-distributed forces was considered during the model development, to provide a closer characterization of the forces exerted on the air in the vicinity of the rotor. Consecutively, a set of test cases is considered for a regularized line force distribution of thrust, with an equivalent integrated value corresponding to the previously prescribed force singularity. The distribution was adapted from existing surface load data of a wing-tip mounted propeller, and its values scaled so that a qualitative relevant acoustic response could be generated. An important detail of line-distributed sources for CAA concerns the constraints posed on the resolvability of sharp source gradients, due to grid cells size requirements for acoustic simulations. As an example, typical load distributions on propeller blades present a sharp gradient at the tip, due to the finiteness of the blade, that requires a finer mesh resolution in order to capture appropriately the flow physics in this region of the blade, as seen in Fig. 8. Since the mesh resolution for CAA computations is bounded to resolve only the desired wavelengths, the generated grid is generally coarser than its typical computational fluid dynamics counterpart, posing an issue in determining a suitable grid refinement for an appropriate representation of the regularized source load distribution.

Therefore, two strategies for resolving tip force gradients on an acoustic grid were considered. Both strategies include the combination of a Gaussian kernel filter on the original distribution, with a value of ε equal to the one used for source regularization in the CAA grid, followed by a subsequent windowing of the force values using a sinusoidal function dependent on ε, in the regions that would correspond to only the hub or to both the hub and tip area of a real blade. The post-filtering windowing step is included to ensure $L1$ continuity of the filtered line source distribution.

The Gaussian kernel filter is defined as in Eq. (22):

$$K(r,\xi) = \exp\left(\frac{-ln(2)|r-\xi|^2}{\varepsilon^2}\right) \tag{22}$$

where ξ represents the integration variable of the applied convolution, and r the line source distribution radial coordinates.

The filtered source is then determined from Eq. (23) as:

$$\boldsymbol{S}(r)_{Filtered} = \int_{-\infty}^{\infty} \boldsymbol{S}(\xi) * K(r,\xi)\, d\xi \tag{23}$$

The windowing procedure is applied to $\boldsymbol{S}(r)_{Filtered}$ at either the corresponding hub or tip region of a real blade, and it is described by Eq. (24).

$$w(r) = \begin{cases} 0, & r < r_{start} \\ 1, & r > r_{end} \\ \sin^2(\pi/2 * (r - r_{start})/(r_{end} - r_{start})), & \text{otherwise} \end{cases} \tag{24}$$

where r_{start} and r_{end} define the line distribution radial extent over which the windowing function $w(r)$ is applied, and $r \in [r_{start}, r_{end}]$ is a coordinate within the specified range. The windowed line-distributed source values are obtained from Eq. (25):

$$\boldsymbol{S}(r)_{Windowed} = \boldsymbol{S}(r)_{Filtered} * w(r) \tag{25}$$

The first strategy, referred to as Pre-Processing Option 1, considers a Gaussian kernel filter $K_{Opt1}(r_{OrigSrc}, \xi)$ defined from Eq. (22), with the radial coordinates r corresponding to the original line source distribution radial coordinates $r_{OrigSrc}$. The filtered source $\boldsymbol{S}(r_{OrigSrc})_{Filtered,Opt1}$ is calculated with Eq. (23), where $r = r_{OrigSrc}$. The subsequent windowing procedure is applied both at the tip and hub regions of the line-distributed source. The window function of the hub region is defined with $r_{start,Opt1} = 0$ corresponding to the minimum radial location of $\boldsymbol{S}(r_{OrigSrc})_{Filtered,Opt1}$, and $r_{end,Opt1} = 2 * \varepsilon$. At the tip region, $w(r)$ is applied with $r_{end,Opt1} = r_{Max}$ corresponding to the maximum radial location r_{Max} of $\boldsymbol{S}(r_{OrigSrc})_{Filtered,Opt1}$, and $r_{start,Opt1} = r_{Max} - 2 * \varepsilon$.

The second strategy, referred to as Pre-Processing Option 2, considers a Gaussian kernel filter $K_{Opt2}(r_{SonicCylLoc}, \xi)$ defined as in Eq. (22), with the radial coordinates $r = r_{SonicCylLoc}$ defined as linearly spaced locations in a range $[0, r_{SonicCyl}]$, where $r_{SonicCyl}$ is the radius of the sonic cylinder. The filtered source $\boldsymbol{S}(r_{SonicCylLoc})_{Filtered,Opt2}$ is calculated with Eq. (23), where $r = r_{SonicCylLoc}$. In this option, the Gaussian kernel filter is applied extending the maximum radius of the original line until a value determined by suitable physical reasoning.

The motivation for the increased radial extent is a consequence of the convolution applied with Eq. (23). In order to realize a smooth source gradient at the tip of the line distribution, with the constraint of maintaining an equivalent half-width value ε to the original line distribution, the radial source coordinates would necessarily increase. To define the maximum extent of the filtered loads values, it is considered that for both compressible and incompressible flow conditions, the pressure field in close proximity to the blade would be bounded to it, and its near-field perturbations would propagate due to the forced motion the air is subject to, as a reaction to the motion of the blade. The near-field perturbations would decay fast enough so that they would not contribute to sound propagation in the far-field region. In addition to that, for a subsonic rotor it would always be possible to trace back the origin of the far-field sound signal as originating from the surface of the sonic cylinder, defined as the cylinder of radius $r_{SonicCyl} = a_\infty/(2n\pi)$ where an hypothetical blade of a subsonic rotor would reach $M_{tip} = 1$. The cylinder of radius $r_{SonicCyl}$ would therefore identify the region in space where near-field perturbations are confined. Since the result of Eq. (23) could determine supersonic source velocities, an appropriate upper radial extension limit needs to be guaranteed, to avoid an excessive modification of the physics involved, relaxing at the same time the source-dependent grid constraints. By extending the line source distribution beyond the original rotor tip up to $r_{SonicCyl}$, and ensuring that the additional resulting load is a minor percentage of the integrated load value of the distribution, the extra forces introduced would produce a rapidly decaying sound signal of a near-field type. At the surface of the sonic cylinder negligible loads values would be realized, thus preventing an excessive manipulation of the original prescribed line distribution. As a consequence of the previous reasoning, the definition of the maximum extent of the filtered line distribution is proposed as the radius $r_{SonicCyl}$ of the sonic cylinder.

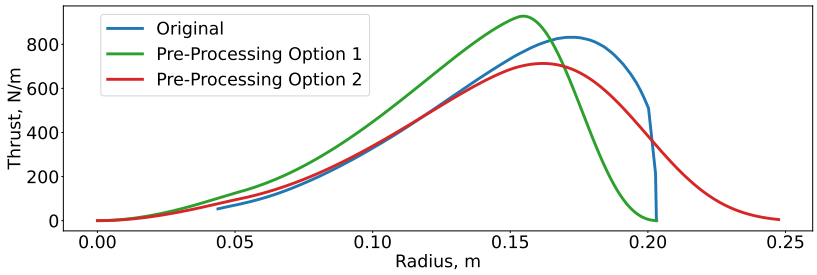

Fig. 8 Thrust distributions for the line-distributed source test cases.

After the filtering procedure, the window function $w(r)$ of Pre-Processing Option 2 is applied only at the hub region of the line-distributed source, with $r_{start,Opt2} = 0$ corresponding to the minimum radial location of $\boldsymbol{S}_{Filtered,Opt2}$, and $r_{end,Opt2} = 2 * \varepsilon$. After performing both smoothing strategies, the distributions obtained are rescaled to maintain the same original integrated thrust value.

In Fig. 8, the original distribution as well as the distributions obtained from the two smoothing criteria defined above, are reported. The smoothing criteria Pre-Processing Option 2 realizes at the tip region a load contribution corresponding to only 6% of the overall integrated force.

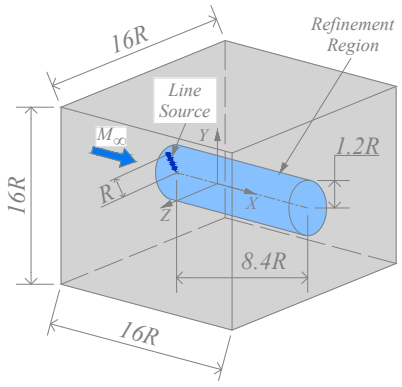

Fig. 9 Computational domain for the line-distributed source test cases

Table 2 Simulations input parameters

Input Parameter	Value
Free-stream Mach nr. M_∞	0.17
n	218.77 s^{-1}
Propeller Blade Length R	0.2032 m
Thrust	75.18 N
Farf. Tetra Cell Size Δx_{Far}	0.3224
Refin. Tetra Cell Size Δx_{Ref}	0.03224
Number of Time Steps	200,000
Time Step Size	0.0001

The simulations setup has been defined to match the previous force singularity test cases, using the same computational domain and cylindrical refinement region, and maintaining the grid cells' size defined before. Figure 9 illustrates the mesh domain for these cases. Table 2 reviews the simulation input parameters. A single rotating line-distributed source is defined in a y-z plane centered at $(x, y, z) = (-0.4, -0.15, 0.0)$. The same non-reflecting boundary condition as defined for the force singularity is applied at the domain outer surfaces. The computational time is maintained as corresponding to nearly five complete revolutions of the line distribution. The results are presented in terms of SPL, considering the 1st, 3rd, and 5th frequency mode of the fluctuating pressure signals, recorded with virtual microphones placed on the x-y coordinate plane at a distance of 4R from the origin of the propeller's cylindrical coordinate system.

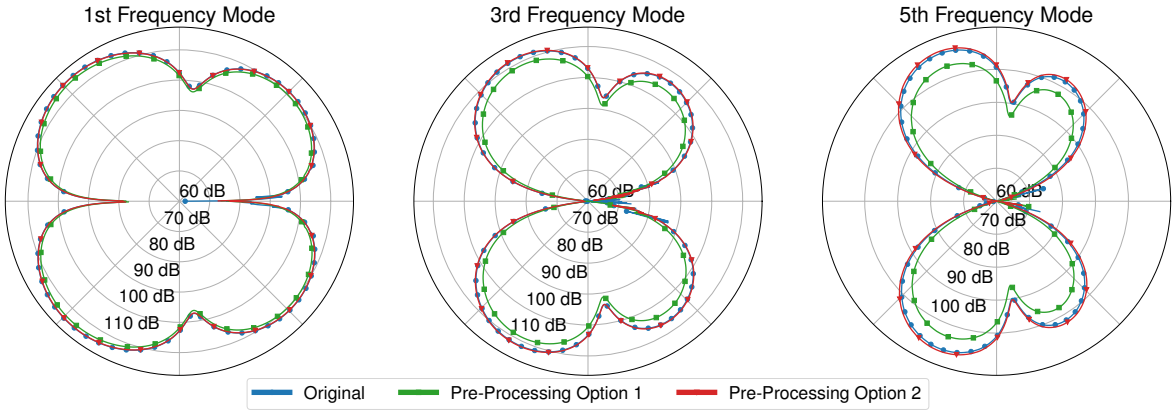

Fig. 10 SPL (dB) for the different thrust distributions, simulated with $M_\infty = 0.17$.

In Fig. 10, the polar directivity results for the smoothing criteria Pre-Processing Option 1 shows an almost constant decrease in SPL values of approximately 3 dB. The windowing-based coefficients applied to the tip-region have a non-negligible effect on the acoustic response, indicating how the definition of the force distribution near the tip-region force contributes predominantly to the generated sound field. This can be identified for all the frequency modes presented. When smoothing according to Pre-Processing Option 2, the pressure signal obtained shows a closer agreement with the original distribution, as it can be identified for the 1st and 3rd frequency mode. The 5th mode presents the larger deviations from the original distribution, indicating how the criteria adopted probably influences most the higher harmonics. From the analysis of the results obtained, the smoothing criteria Pre-Processing Option 2 revealed to be the most promising approach to adequately resolve the force gradients in the corresponding blade tip region, provided that the additional loads created in the area beyond the initial tip constitute a small percentage of the original integrated force, and decay rapidly to very small values.

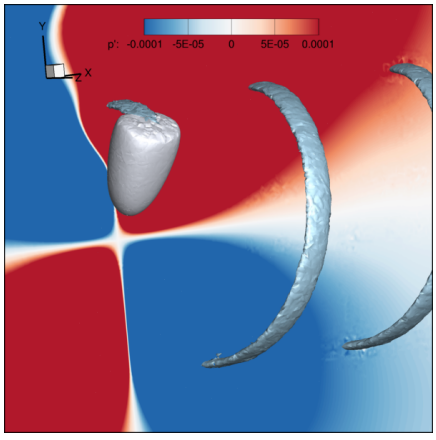

Fig. 11 Contour plot of p' for the original line distribution, with Q-Criterion superimposed

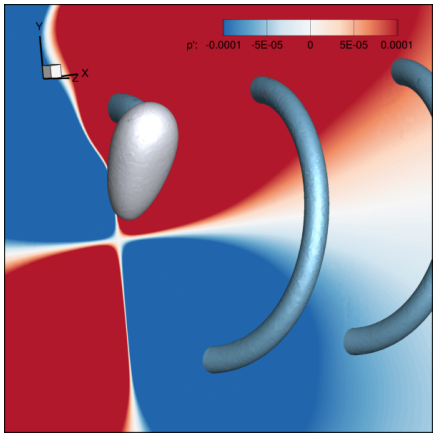

Fig. 12 Contour plot of p' for the Pre-Processing Option 2 distribution, with Q-Criterion superimposed

As a consequence of the smoothing criteria, the generated vortical structures downstream of the propeller would differ qualitatively from the initial distribution, as it can be seen comparing Fig. 11 and 12. The original distribution with sharp source gradients at the tip would produce a tip vortex section having a seemingly ellipsoidal shape, stretched in the propeller axis direction. The Pre-Processing Option 2 smoothing criteria adopted would modify the cross-sectional shape of the vortex into a more round contour, more uniformly distributed in all directions. Nevertheless, the qualitative vortex tube section modification is seen to not influence the acoustic response significantly. A thorough validation of the identified smoothing criteria is planned in the future, to confirm its validity.

C. Installed vs. Isolated Rotor Configuration

At this stage, a practical definition of useful setup criteria has been identified for the regularized source, and the rotor model in combination with the equations will be qualitatively tested with a more realistic setup, involving an adequately defined installed rotor configuration. The corresponding simulations have been defined based on the same thrust distribution as used before, and a suitable torque distribution as well. As a source smoothing criteria, the approach defined as Pre-Processing Option 2 was considered. For the thrust distribution, the additional loads at the extended tip-region amount to 6% of the integrated thrust force, while for the torque distribution the extended loads amount to 7%.

Figures (13) and (14) display the distributions considered, compared to the original input data.

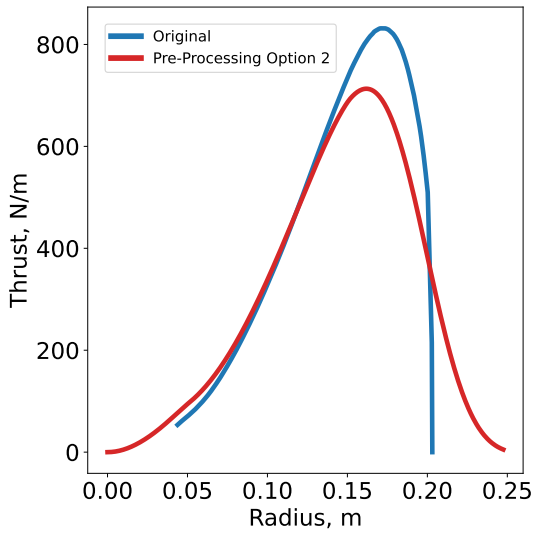

Fig. 13 Thrust distribution for comparison of installed and isolated propeller configurations. Only the red curve distribution is considered for the test cases.

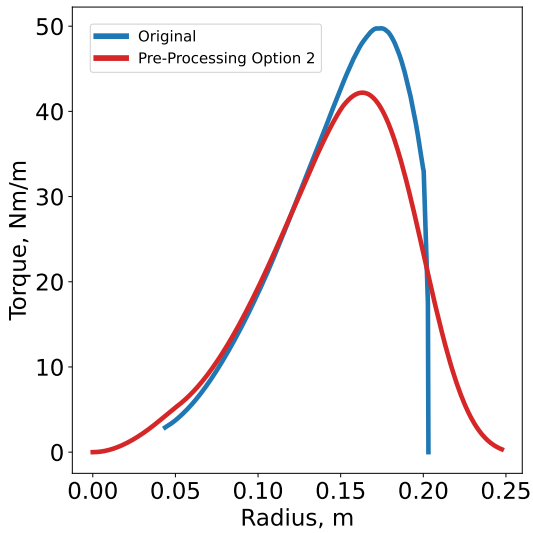

Fig. 14 Torque distribution for comparison of installed and isolated propeller configurations. Only the red curve distribution is considered for the test cases.

As a background mean flow for the installed configuration, a RANS solution obtained for a DU-96-W-180 airfoil profile was considered, with Table 3 summarising its main input parameters. The RANS solution was performed only for the airfoil profile, and does not include the splistream of the corresponding propeller subsequently modelled in the CAA framework. For the isolated configuration, a uniform background mean flow was prescribed, equivalent to the RANS free-stream flow velocity. Table 4 presents the simulation input parameters. Figures (15) and (16) illustrate the computational domain created for both the isolated and installed case. The domain dimensions, as well as the line source radial extension, were scaled with the airfoil chord c.

Three rotating equi-spaced line-distributed sources are defined in a y-z plane centered at $(x, y, z) = (-0.4, -0.15, 0.0)$. The tetrahedral cells size in the farfield of the computational domain is defined to resolve the first five harmonics, and in the refinement region the grid cells size is reduced to 1/10 of the farfield tetrahedral edge length. The non-reflecting boundary condition at the domain outer surfaces is defined as the same one used for the point and line force test cases. The computational time is maintained as corresponding to nearly five complete revolutions of the lines distribution. The wall boundary condition used for the extruded airfoil profile is based on a ghost point approach, where an additional ghost point with identical coordinates as the high order points on tetrahedral faces describing the airfoil surface is added.

Table 3 RANS simulation input data

Input Parameter	Value
Chord Length c	$0.4m$
Reynolds nr. Re	$1.13 * 10^6$
Free-stream Mach nr. M_∞	0.17
Angle of attack α	4°

Table 4 CAA simulations input parameters

Input Parameter	Value
Free-stream Mach nr. M_∞	0.17
n	$218.77\ s^{-1}$
Propeller Blade Length R	$0.2032\ m$
Farf. Tetra Cell Size Δx_{Far}	0.2149
Refin. Tetra Cell Size Δx_{Ref}	0.02149
Number of Time Steps	200,000
Time Step Size	0.0001

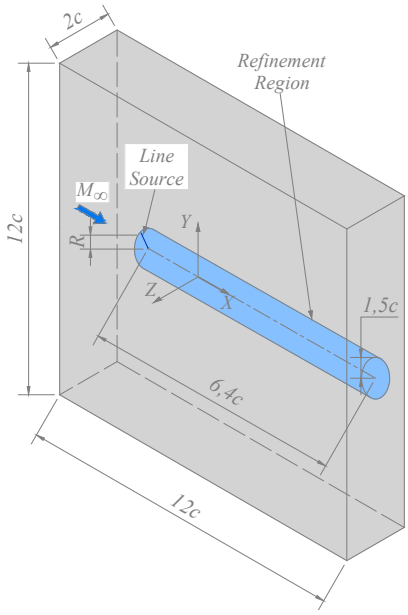

Fig. 15 Computational domain of the isolated propeller configuration

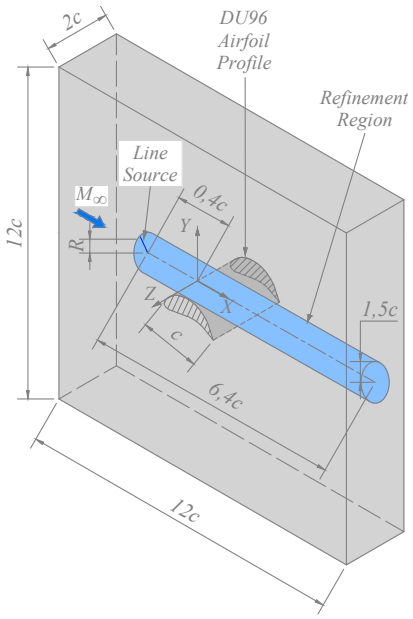

Fig. 16 Computational domain of the installed propeller configuration

At the wall surfaces, the flux is formulated based on an upwind flux vector splitting approach, where the inner tetrahedral cell state is prescribed base on the interior solution, and the ghost point cell state has a slip-wall velocity definition for the potential components $\boldsymbol{u^a}$, and for the non-acoustic component $\boldsymbol{u^r}$ a null prescribed incoming eigenmodes definition. The obtained results are analysed in terms of SPL of the fluctuating pressure signals, considering the polar directivity of the 1st, 3rd, and 5th frequency mode. The solution at two different distances was compared, respectively at 4R for investigating the near-field acoustic, and at 8R for a far-field solution inspection.

A qualitative inspection of the results for both the installed and isolated propeller configuration, as seen in Fig. 17 and Fig. 18, shows how the approach proposed combining the APE+VCE equations system and the rotor source noise model is successful in highlighting the main features to be expected from the simulations considered. The convected line source tip vortices interacting with the wing profile, produce a corresponding change in the acoustic response, as visible from the pressure fluctuations contours level above the wing. The smoothing criteria Pre-Processing Option 2 of the line sources does not produce unwanted instabilities, and is confirmed as a valid method to resolve the problem posed by source gradients non-resolvable with an acoustic mesh. The polar directivity results of the comparison of the isolated and installed configurations for a distance 4R are initially inspected in Fig. 19, showing a considerable increase in SPL along the propeller axis, from −30° to 30°, and from 150° to 210°. It can also be noted that in the region around 45°, the installed configuration produces a visible increase in SPL of nearly 8 dB, whereas for locations from 210° to 330° an almost equivalent decrease in sound levels is detected, of nearly 5 dB.

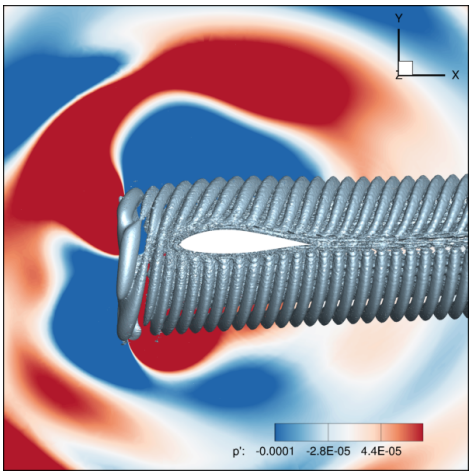

Fig. 17 Contour plot of p' for the installed propeller configuration, with Q-Criterion superimposed

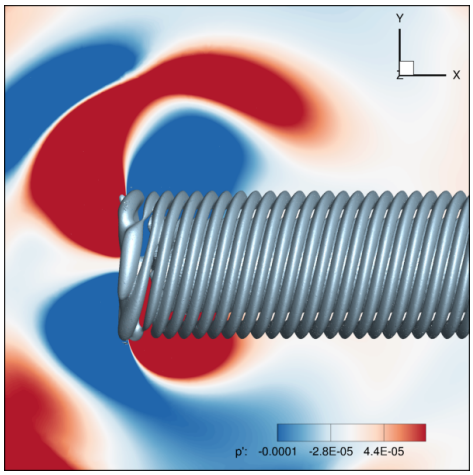

Fig. 18 Contour plot of p' for the isolated propeller configuration, with Q-Criterion superimposed

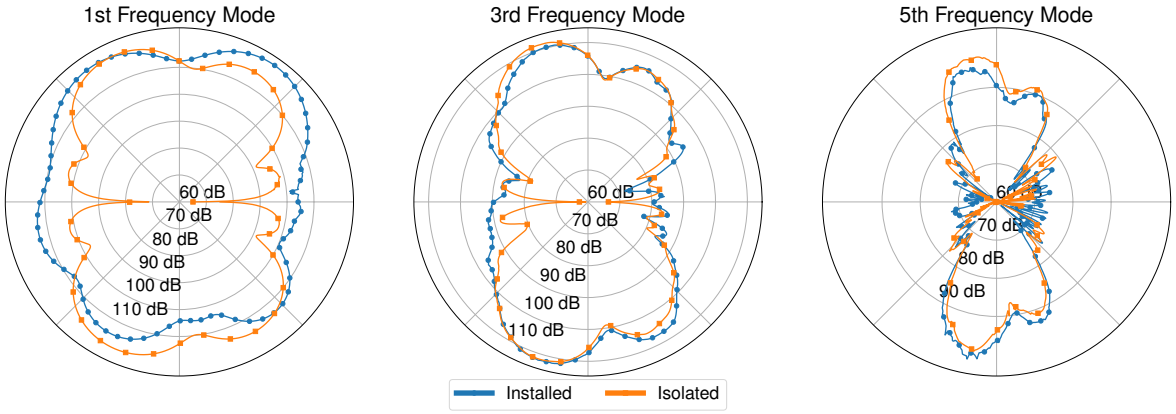

Fig. 19 SPL (dB) for the installed and isolated configurations, at a distance of 4R from the propeller.

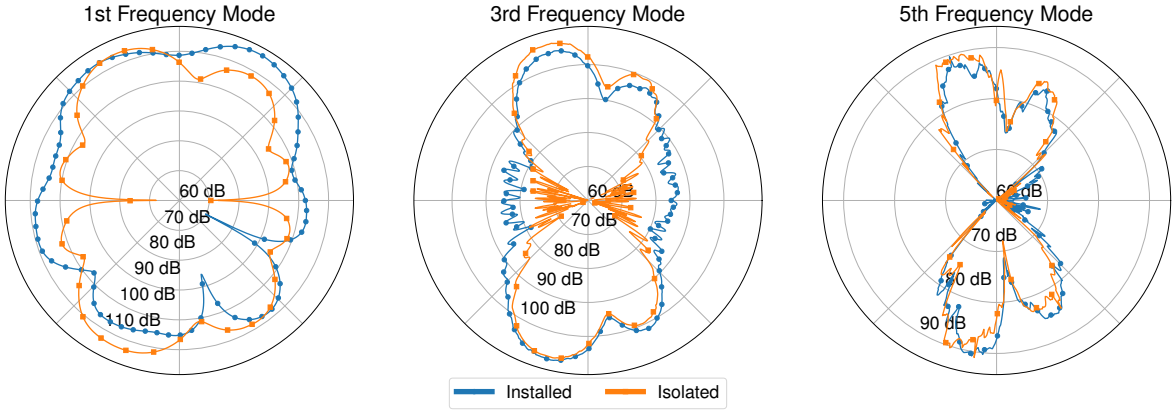

Fig. 20 SPL (dB) for the installed and isolated configurations, at a distance of 8R from the propeller.

For higher modes it can be seen that the difference between installed and isolated cases decreases overall. The comparison of the directivity results at a distance of 8R are shown in Fig. 20. The predominant axial noise identified at a lower distance from the propeller is still visible, as well as the increase of the sound levels in the region around 45°, and the decrease of SPL from 210° to 330°. It becomes visible also a decrease in sound levels at around 330°, which could be attributable to the particular installed configuration setup chosen. The 3rd mode results highlight a considerable increase in axial noise both upstream and downstream of the wing. The 5th mode results do not display any more large detectable differences between isolated and installed configuration. Overall, it can be seen that the particular configuration considered reduces the SPLs propagated below the wing profile, that originate from the interaction of the propeller with the wing profile. A detectable acoustic response is seen to be present only for the 1st frequency mode, whereas for higher modes the sound field generated from the propeller interaction at the leading edge probably compensates partially the sound field generated from the propeller.

V. Conclusion

A new method for noise prediction of installed rotors was developed in a CAA framework, including regularized source singularities as well as line-distributed sources, in combination with the newly proposed APE+VCE system of perturbation equations. The proposed method aims to reduce, at an acceptable level of accuracy, the computational cost of CAA simulations for rotor noise estimation, in order to investigate installation noise. The APE+VCE system of equations successfully overcomes physical and numerical instabilities that characterize the LEE. The stability of the APE+VCE in the DG framework is further improved by application of suitable limiter formulations, defining a robust application-oriented method. Initial results of this approach show the expected trends and patterns of the predicted fluctuating pressure signal. SPLs of simulated thrust distributions capture the essential noise prediction features, in both a uniform background medium and more realistic installed rotor configurations. As a future development, numerical noise mitigation techniques will be included to fine-tune the model, and validation against experimental data will be considered as well.

Acknowledgments

We would like to acknowledge the funding by the Deutsche Forschungsgemeinschaft (DFG, German Research Foundation) under Germany's Excellence Strategy –EXC 2163/1-Sustainable and Energy Efficient Aviation –Project-ID 390881007.

References

[1] Gohardani, A. S., Doulgeris, G., and Singh, R., "Challenges of future aircraft propulsion: A review of distributed propulsion technology and its potential application for the all electric commercial aircraft," Progress in Aerospace Sciences, Vol. 47, No.5, 2011, pp. 369, 391. https://doi.org/10.1016/j.paerosci.2010.09.001

[2] Wall, T. J., Meyer, R. T., "A Survey of Hybrid Electric Propulsion for Aircraft," 53rd AIAA/SAE/ASEE Joint Propulsion Conference, AIAA, Atlanta, GA, 2017. https://doi.org/10.2514/6.2017-4700

[3] Gutin, L., "On the Sound Field of a Rotating Propeller," NACA TM-1195, 1948.

[4] Lowson, M. V., and Lighthill, M. J., "The sound field for singularities in motion," Proceedings of the Royal Society of London, Vol. 286, No. 1407, 3 Aug. 1965, pp. 559–572. https://doi.org/10.1098/rspa.1965.0164

[5] Hanson, D. B., "Influence of Propeller Design Parameters on Far-Field Harmonic Noise in Forward Flight," AIAA Journal, Vol. 18, No. 11, Nov. 1980, pp. 1313–1319. https://doi.org/10.2514/3.50887

[6] Peake, N., Crighton, D., "An asymptotic theory of near-field propeller acoustics," Journal of Fluid Mechanics, Vol. 232, Nov.1991, pp. 285–301. https://doi.org/10.1017/S0022112091003695

[7] Smith, M., "A Prediction Procedure for Propeller Aircraft Flyover Noise Based on Empirical Data," SAE Technical Paper 810604, Feb. 1981. https://doi.org/10.4271/810604

[8] Lewy, S., "Semi-empirical prediction of tone noise due to counter-rotating open rotors," Proceedings of 20th International Congress on Acoustics, Aug. 2010. URL:https://www.acoustics.asn.au/conference_proceedings/ICA2010/cdrom-ICA2010/papers/p113.pdf

[9] Tanna, H. K., Burrin, R. H., and Plumblee, H. E., "Installation effects on propeller noise," Journal of Aircraft, Vol. 18, No. 4, Apr. 1981, pp. 303–309. https://doi.org/10.2514/3.44703

[10] Shivashankara, B., Johnson, D., and Cuthbertson R., "Installation effects on counter rotating propeller noise," 13th Aeroacoustics Conference, AIAA, Tallahassee, FL, Oct. 1990. https://doi.org/10.2514/6.1990-4023

[11] Sinnige, T., Ragni, D., Eitelberg, G., and Veldhuis L. L. M., "Mitigation of Pusher-Propeller Installation Effects by Pylon Trailing-Edge Blowing," Journal of Aircraft, Vol. 54, No. 1, Jan. 2017, pp. 292–300. https://doi.org/10.2514/1.C034000

[12] Romani, G., Ye, Q., Avallone, F., Ragni, D., and Casalino D., "Numerical analysis of fan noise for the NOVA boundary-layer ingestion configuration," Aerospace Science and Technology, Vol. 96, Jan. 2020. https://doi.org/10.1016/j.ast.2019.105532

[13] Tam, C. K. W., "Computational Aeroacoustics: An Overview of Computational Challenges and Applications," International Journal of Computational Fluid Dynamics, Vol. 18, No. 6, 2004, pp. 547–567. https://doi.org/10.1080/10618560410001673551

[14] Goldstein, M. E., "Unsteady vortical and entropic distortions of potential flows round arbitrary obstacles," Journal of Fluid Mechanics, Vol. 89, No. 3, 1978, pp. 433–468. https://doi.org/10.1017/S0022112078002682

[15] Hunt, J. C. R., "A theory of turbulent flow round two-dimensional bluff bodies," Journal of Fluid Mechanics, Vol. 61, No. 4, 1973, pp. 625–706. https://doi.org/10.1017/S0022112073000893

[16] Kerrebrock, J. L., "Small disturbances in turbomachine annuli with swirl," AIAA Journal, Vol. 15, No. 6, 1977, pp. 794–803. https://doi.org/10.2514/3.7370

[17] Atassi, H. M., and Golubev, V. V., "Unsteady Disturbances in Swirling Turbomachinery Flows," Unsteady Aerodynamics and Aeroelasticity of Turbomachines, edited by T.H. Fransson, Springer, Dordrecht., 1998. https://doi.org/10.1007/978-94-011-5040-8_10

[18] Logue, M., and Atassi, H., "Scattering of Acoustic Waves by a Rotor," 14th AIAA/CEAS Aeroacoustics Conference, AIAA, Vancouver, CA, 2008. https://doi.org/10.2514/6.2008-2989

[19] Logue, M., and Atassi, H., "Sound Generation and Scattering from a Rotor in Nonuniform Flow," 16th AIAA/CEAS Aeroacoustics Conference, AIAA, Stockholm, SE, 2010. https://doi.org/10.2514/6.2010-3743

[20] Cooper, A., and Peake, N., "Analytically-based Approach to Rotor-stator Interaction Noise in Mean Swirling Flow," 10th AIAA/CEAS Aeroacoustics Conference, AIAA, Manchester, GB, 2004. https://doi.org/10.2514/6.2004-2996

[21] Lloyd, A., and Peake, N., "Rotor-Stator Broadband Noise Prediction," 14th AIAA/CEAS Aeroacoustics Conference, AIAA, Vancouver, CA, 2008. https://doi.org/10.2514/6.2008-2840

[22] Wohlbrandt, A. M., Guérin S., Ewert, R., "Simultaneous Computation of Surface and Volume Sources for Fan Broadband Noise with the Random-Particle-Mesh Method," 19th AIAA/CEAS Aeroacoustics Conference, AIAA, Berlin, DE, 2013 https://doi.org/10.2514/6.2013-2119

[23] Ewert, R., and Kreuzinger, J., "Hydrodynamic/acoustic splitting approach with flow-acoustic feedback for universal subsonic noise computation," Preprint submitted to Journal of Computational Physics, 2020. URL:https://arxiv.org/abs/2009.07155

[24] Ewert, R., and Schroeder, W., "Acoustic perturbation equations based on flow decomposition via source filtering," Journal of Computational Physics, Vol. 188, No. 2, 2003, pp. 365–398. https://doi.org/10.1016/S0021-9991(03)00168-2

[25] Dierke, J., Akkermans, R. A., Delfs, J. W., and Ewert, R., "Installation Effects of a Propeller Mounted on a Wing with Coanda Flap. Part II: Numerical Investigation and Experimental Validation," 20th AIAA/CEAS Aeroacoustics Conference, Atlanta, GA, 2014. https://doi.org/10.2514/6.2014-3189